Proceedings of 2004 Korea-Japan Joint Seminar
on Particle Image Velocimetry
POSTECH, Korea, Dec. 9 - 10

# Scanning Stereoscopic PIV for 3D Vorticity Measurement

Jun SAKAKIBARA and Toshio HORI

Department of Engineering Mechanics and Energy
University of Tsukuba
Tennodai 1-1-1, Tsukuba, Ibaraki, 305-8573, Japan
*sakakiba@kz.tsukuba.ac.jp*

***Abstract:*** A scanning stereo-PIV system was developed to measure the three-dimensional distribution of three-component velocity in a turbulent round jet. A laser light beam produced by a high repetition rate YLF pulse laser was expanded vertically by a cylindrical lens to form a laser light sheet. The light sheet is scanned in a direction normal to the sheet by a flat mirror mounted on an optical scanner, which is controlled by a programmable scanner controller. Two high-speed mega-pixel resolution C-MOS cameras captured the particle images illuminated by the light sheet, and stereoscopic PIV method was adopted to acquire the 3D-3C-velocity distribution of turbulent round jet in an octagonal tank filled with water. The jet Reynolds number was set at $Re = 1000$ and the streamwise location of the measurement was fixed at approximately $x = 40D$. Time evolution of three-dimensional vortical structure, which is identified by vorticity, is visualized. It revealed that the existence of a group of hairpin-like vortex structures was quite evident around the rim of the shear layer of the jet. Turbulence statistics shows good agreement with the previous data, and divergence of a filtered (unfiltered) velocity vector field was 7% (22%) of root-mean-squared vorticity value.

***Keywords:*** Scanning Stereo-PIV, three-dimensional measurement, round jet, vortical structure, turbulence

## 1. Introduction

One of the most desirable velocimetries is one that can resolve time-dependent three-dimensional three-component velocity vectors in a complex turbulent flow field. Such a method would enable us to obtain all the elements of the velocity gradient tensor, thus allowing the turbulent structures to be visualized by an appropriate vector or scalar such as vorticity or the second invariant of the velocity gradient tensor. Several methods of three-dimensional velocimetry have been presented thus far. Three-dimensional particle tracking velocimetry (3D-PTV), which tracks individual tracer particles using multiple cameras, has been used for several decades (Chiu & Rib (1956); Nedderman (1961)). Racca and Dewey (1988) measured the 3D velocity of tracer particles seeded in a water flow inside a square duct by using a 16-mm high-speed cine-camera. Within a decade, the film-based camera was replaced by modern CCD cameras as imaging devices for 3D-PTV. Nishino *et al.* (1989) developed a 3D-PTV system consisting of three TV cameras. Their Measurements of decaying turbulence in a stirred water tank demonstrated that their technique could be applied to turbulent flows. Since individual particles were identified and tracked with 3D-PTV, the interrogation spot size was relatively smaller than that with regular PIV and thus the technique was robust against the higher shear rate of the flow field. However, each particle has to be sparsely distributed in a measurement volume to identify it in a three-dimensional volume, and the typical number of instantaneous velocity vectors in a volume is on the order of a hundred, which is not sufficient to compute the spatial derivative of velocity. Note that the density of 2D-PTV has been significantly

improved (Stitou and Riethmuller (2001)) to the extent, where the three-dimensional location of each particle does not necessarily have to be distinguished.

Particle image velocimetry (PIV) is now commonly used for measuring 2- or 3-velocity components in 2D slices of the velocity field. Since the particles are densely seeded, the number of velocity vectors measured is larger than that with PTV and more feasible for obtaining the spatial derivative of velocity than with PTV. However, it has been difficult to identify thus 3D position of each particle, and thus 3D volumetric measurement has not been available except through holographic PIV (Zhang *et al.* (1997)), which requires a considerably complex optical system. One possible way of extending 2D-PIV to 3D volumetric measurement is with PIV using a fast scanning light sheet. Ushijima and Tanaka (1996) developed a scanning 3D-PIV system that visualizes an entire three-dimensional flow field with scanning laser-light sheets generated from a pair of optical scanners. The technique was applied to rotating fluids accompanied by Ekman boundary layers. Brucker (1995) measured multiple 2D slices of a 2-velocity-component with scanning PIV employing one video camera, and evaluated the out-of-plane component of velocity by integrating the continuity equation. This method, however, can only be applied in flows for which the third velocity component is known at the boundary of the integration domain. He presented another technique such as scanning stereo PIV, which requires two video cameras viewing the same measurement region from different directions to evaluate the out-of-plane component of velocity (Brucker (1996)). He used two regular CCD cameras with a frame rate of 25 Hz and a scanning laser light sheet, and measured the wake flow behind the spherical cap at $Re$ = 100. Since the frame rate was low, the slices in the measurement volume were limited to 9, which was not sufficient for the higher $Re$ flow occupied by the finer scale of eddies.

In the present study, we describe a scanning stereo PIV system capable of higher spatial resolution that resolves eddies in a turbulent flow field at $Re \approx 1000$. Two high-speed mega-pixel resolution C-MOS cameras and a high repetition pulse laser were used to construct the system. Light sheet scanning was achieved with a fast optical scanner. We could measure a fully developed turbulent jet with the system, and were able to visualize 3D vortical structures. Although a part of the present study was recently published in a reference (Hori & Sakakibara, 2004), turbulence statistics, those were endorsed high reliability by long term measurement, were computed from the 3D velocity field which were newly obtained.

# 2. Method

It is now common in standard non-scanning stereo PIV for the laser light sheet to be adjusted to fit on the surface of the calibration plate placed on the plane to be measured. Once the calibration procedure was performed on this calibration plate, the projection of the physical location of any point (although limited in view) in the light sheet plane to the image coordinate is known based on the mapping function obtained from the calibration procedure. Similar calibration can be done with scanning PIV such that the calibration plate can be placed on any plane the light sheet illuminates during scanning. However, this method requires considerable time to set the calibration plate on the many planes to be measured. Also, a complicated traversing mechanism is needed to place the calibration plate within the light sheet planes, if they are not parallel to one another as in the present setup. Because of these difficulties, we proposed a new method that is suitable for scanning PIV, which we will describe in the sections that follow.

## *2.1 Flow Apparatus and Experimental Conditions*

Figure 1 outlines the flow apparatus for a turbulent round jet. Water in the overhead tank was introduced to a honeycomb flow straightener and axisymmetric contraction nozzle having a 5 mm exit diameter, $D$. The nozzle was figured smoothly in a 3rd order polynomial curve, and the downstream end of the nozzle was mounted beneath the bottom plate of a 500-mm-high Plexiglas octagonal tank, with 400 mm between the opposing sidewalls. This configuration created an initially laminar jet with a top hat velocity profile issuing upward into the octagonal tank. The water in the tank overflowed through four equally spaced drainpipes mounted 450 mm from the bottom surface of the tank. The water was then returned to the overhead tank with a hydro pump. The bulk velocity at the exit of the nozzle was $U_0 = 225$ mm/s, and the corresponding jet Reynolds number was $Re = U_0 D/\nu = 1036$ , where $\nu$ is kinematic viscosity.

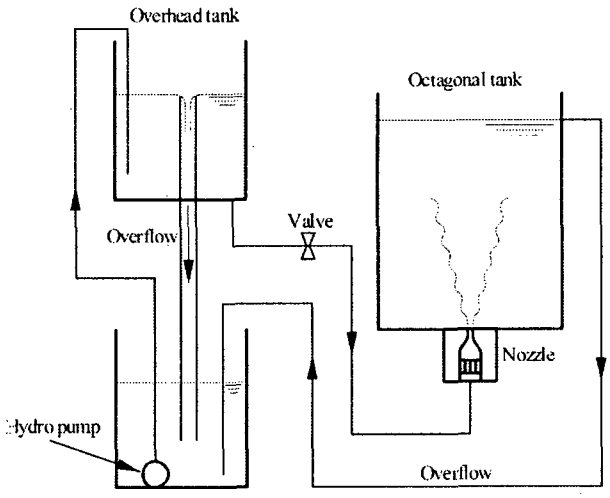


Figure 1. Flow apparatus

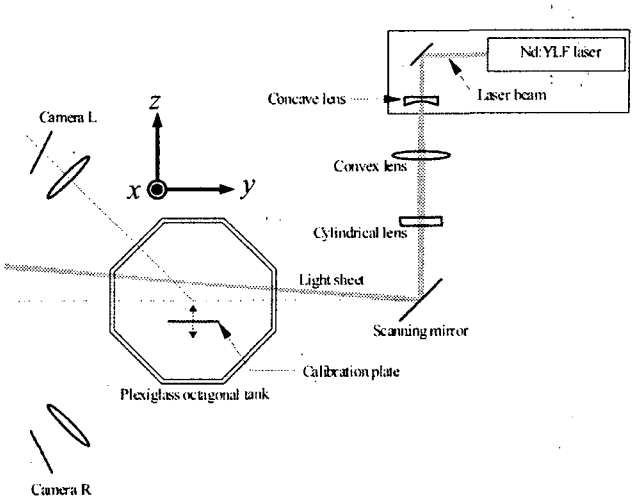


Figure 2. Optical arrangement

## 2.2 Hardware Setup

The optical configuration is shown in figure 2. The laser light beam emitted from a diode-pumped Nd:YLF pulse laser ( 20 mJ per pulse at 2000 Hz, Evolution 30, Positive Light ) was converged through a pair of spherical lenses ( $f$=-150 and 200 mm ) and expanded vertically through a cylindrical lens ( $f$=-70 mm ) to form a 2-mm-thick laser light sheet at the test section. The light sheet was scanned with a flat mirror mounted on an optical scanner ( VM2000, GSI Lumonics ), which is controlled with a programmable scanner controller ( SC2000, GSI Lumonics ).

Tracer particles ( 40 μm Polyamid 12, Daiamid 2157, Daicel Degussa ) were seeded in the flow, and scattered light was imaged with two high-speed high-resolution C-MOS cameras ( 2000 fps with 1024 × 1024 pixels resolution in maximum, Fastcam APX, Photron ). Camera L was placed at the left of the light sheet plane toward the laser source, and the angle of the camera axis with respect to the light sheet plane was set at approximately 45°. This was also done for camera R at the right. Both cameras could then detect stronger forward scattering light from the particles compared to weaker side or back scattering, with a smaller lens aperture, i.e., a higher f-number of 22, which provided a greater depth of field.

Each camera was tilted with respect to the lens axis to satisfy the Scheimpflug condition and was focused at the center of the measurement volume. The center of measurement volume ( 100×100×100 $mm^3$ ) was located 40$D$ above the nozzle on the jet centerline, which was 800 mm from the axis of the scanning mirror. Images captured with the cameras were recorded in their memory, and then transferred to a PC hard disk.

The calibration plate was made of flat aluminum and had through hole arrays of 1.5 mm in diameter at 5 mm intervals to provide the same calibration target pattern on both sides for each camera. The plate was 150 mm wide, 500 mm long and 5 mm thick, and was installed vertically on a servo-motor-driven traversing mechanism ( Robo-cylinder, IAI ) with a traversing accuracy of 20 μm. The plate was perpendicular to the traversing direction. The Cartesian coordinates with $x$ in the jet's streamwise (vertical) direction, $z$ in the direction normal to the plate, $y$ in the other direction, and the origin at the center of the nozzle exit were defined. Also $u$, v and $w$ denote $x$, $y$ and $z$ component of velocity vector, respectively. Note that the rotation axis of the optical scanner was aligned precisely parallel to the $x$-axis.

## 2.3 Measurement of Light Sheet Position

After setting up the imaging hardware, the physical location of the light sheet planes for a given angle of the mirror scanner had to be determined. Figure 3 outlines the geometry of the light sheet and calibration plate. The rotation axis of the laser light sheet, which was parallel to the $x$-axis, was centered at ($y_c$, $z_c$) = (1483.2 mm, 182.0 mm) on the $y$-$z$ plane. The angle of light sheet $\theta$ with respect to the $y$-axis and the angle of scanner mirror $\varphi$ were also defined. Here, the rotation axis of the scanning mirror does not coincide with the rotation axis of the laser light

sheet since rays are refracted on the air/Plexiglas/water interface. The equation for the light sheet plane at any given mirror angle was determined in the following way: The scanning mirror was set at angle $\varphi_A$, where the light sheet remained at one edge of the measurement volume. The calibration plate was then precisely traversed to position $z=z_I$.

Next, an image of the plate, which was illuminated by light sheet., was recorded. A point $P_I$ that was a center of the light sheet hitting on the plate was measured by processing this recorded image. Light intensity distribution on the plate is assumed as

$$I = I_0 \exp\{-a(y-y_I)^2\}. \tag{1}$$

Where, $I$ is recorded intensity of light on the plate, $I_0$ is maximum intensity, and $y_I$ is a centerline where light hitting on. Physical position $y$ that corresponds to image intensity $I$ in the image coordinate could be obtained by 2D-2D calibration technique as shown below (Section 2.6). Producing a table of intensity and physical position on the plate by this method, coefficients $I_0$, $a$, $y_I$ were obtained by least-squares method. Thus, the physical position of $P_I$ could be obtained as $P_I = (y_I, z_I)$.

Next, the calibration plate was slightly traversed to another position of $z=z_{II}$ to hit the light sheet at another point $P_{II}$, and the point $P_{II} = (y_{II}, z_{II})$ was measured in the same manner. Using this set of points, the following equation for this light sheet plane was obtained;

$$c_1^A y + c_2^A z = 1. \tag{2}$$

The same procedure was repeated for another mirror angle $\varphi_B$, where the light sheet remained at the other edge of the measurement volume, allowing an equation for the other plane to be obtained.

$$c_1^B y + c_2^B z = 1. \tag{3}$$

The angles of these two planes with respect to the $y$-axis are given as

$$\theta_A = \tan^{-1}(-c_1^A / c_2^A) \tag{4}$$

and

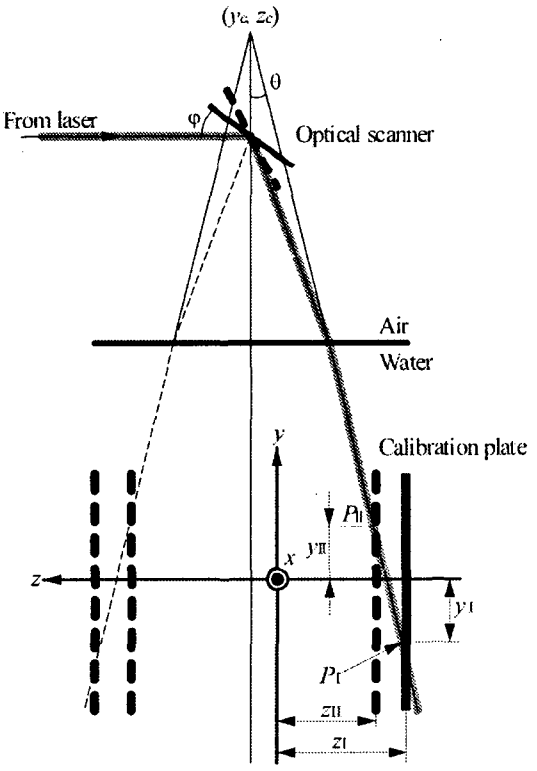


Figure 3. Schematic of light sheet plane viewed from top.

$$\theta_B = \tan^{-1}(-c_1^B / c_2^B) \tag{5}$$

for $\varphi_A$ and $\varphi_B$, respectively. Thus, the angle of light sheet $\theta$ at a given mirror angle of scanner $\varphi$ was formulated in terms of linear interpolation as

$$\theta = \frac{\varphi - \varphi_A}{\varphi_B - \varphi_A}(\theta_B - \theta_A) + \theta_A \cdot \tag{6}$$

Finally, the equation for the light sheet plane at any given angle $\theta$ was defined as

$$c_1(\theta) y + c_2(\theta) z = 1, \tag{7}$$

where the coefficients were calcurated as

$$\begin{pmatrix} c_1(\theta) \\ c_2(\theta) \end{pmatrix} = \begin{pmatrix} \cos(\theta - \theta_A) & -\sin(\theta - \theta_A) \\ \sin(\theta - \theta_A) & \cos(\theta - \theta_A) \end{pmatrix} \begin{pmatrix} c_2^A \\ c_2^A \end{pmatrix}. \tag{8}$$

## *2.4 Scanning Mirror Control and Synchronization*

The particle images required to obtain the volumetric velocity distribution at one instance with our scanning stereo PIV consisted of a series of PIV images taken at successive light sheet planes stacked in the azimuthal direction of the light sheet scan. Each PIV image was a pair of particle images separated by time $\Delta t$, and successive light sheet planes were separated in the azimuthal direction by angle $\delta\theta$. Each step in the mirror's angle corresponding to $\delta\theta$ was defined as;

$$\delta\varphi = \frac{\varphi_B - \varphi_A}{\theta_B - \theta_A}\delta\theta. \tag{9}$$

Here, $\Delta t$=18 ms was needed to ensure sufficient particle displacement ($\approx$ 10 pixels) in the images. However, this interval was too short to scan the light sheet completely in the measurement volume due to limitations with the camera's maximum frame rate. However, this interval was too long to leave the light sheet at a single location, resulting in insufficient scanning speed. We thus propose following scanning scheme.

The mirror is placed at initial position $\varphi = \varphi_0$, and the laser is emitted. Then, the particle images are captured at time $t = 0$. The mirror is then rotated to $\varphi = \varphi_0 + m\delta\varphi$ at $t = \delta t$, where $m$ is an integer value, and $\delta t$ is the frame interval of the camera, which is identical to the inverse of the camera's frame rate, $f_c$. Next, the light sheet is moved to $\varphi_0+\delta\varphi$, and continues in a series such as $\varphi_0+(m+1)\delta\varphi$, $\varphi_0+2\delta\varphi$, $\varphi_0+(m+2)\delta\varphi$, ..., $\varphi_0+(n-1)\delta\varphi$, $\varphi_0+(n-1+m)\delta\varphi$, $\varphi_0+n\delta\varphi$, $\varphi_0+(n+m)\delta\varphi$, where $n$ denotes the number of measurement planes in a measurement volume. With this motion, the location of the light sheet at any time $t$ is identical to its location at time $t+(2m-1)\delta t$. The example of the evolution of $\varphi$ in figure 4 is referred to in the next paragraph. Thus, the images captured at these two sheet locations, separated by $\Delta t=(2m-1)\delta t$, were used as a PIV image pair at each measurement plane. This allowed more freedom to set $\Delta t$ to an appropriate value independent of the frame rate. We selected $n$=50, $m$=5, $\delta\varphi$=0.12° and $\delta\theta$=0.07° for the present study.

To synchronize the optical equipment, trigger pulses were generated by a digital pulse/delay generator (DG535, Stanford Research) to send signals to the cameras, the laser, and the optical scanner. Figure 4 is a timing chart of the signals. Table 1 lists actual settings for the imaging hardware.

A master clock with a frequency of $f_c$=500 Hz generated by the digital delay/pulse generator was sent to both cameras to trigger the exposures. Thus, the cameras were operated at a frame rate of 500 fps. A delayed clock, which lagged 1 ms behind the master clock, was sent to trigger the laser. The signal ``Trigger for recording" was manually sent at arbitrary times to the cameras. The cameras actually started recording after this signal was received. This signal and the delayed clock were also sent to the scanner controller, which begins to rotate the mirror to the next angle immediately after every leading edge of the delayed clock, unless the signal ``Trigger for recording" was on. Thus, the laser and the cameras were initially running at frequency $f_c$, and immediately after manually turning on the ``Trigger for recording" signal, image recording and mirror scanning both started. The frame rate of 500 fps was 1/4 of the maximum frame rate of our cameras, since the optical scanner could not realize the expected motion above this frame rate with the present configuration.

Note that the time required to scan the light sheet over the measurement volume became $T_s = 2(n+m-1)/f_c = 0.216$ s, and also the time required to bring the light sheet back to the initial position was $T_r = 0.230$

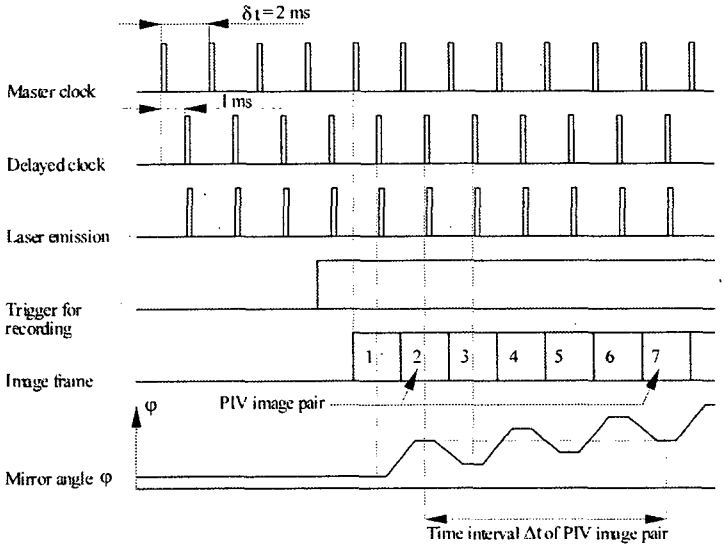


Figure 4. Time chart for signals and operation. $m$ is 3 in this time chart for simplicity.

s. Thus, the time interval between successive volumetric data was $\Delta T = T_s + T_r = 0.446$ s. The spatial interval between adjacent light sheet planes (or measurement planes) was $\Delta z = 2.0$ mm at the center of the measurement volume.

## *2.5 Interrogation*

Let us now consider measuring the velocity at a given point $(x, y)$ on a light sheet plane at angle $\theta$. Referring to equation (7), dependent variable $z$ is simply determined by

$$z = \frac{1 - c_1^{\theta} y}{c_2^{\theta}}. \tag{10}$$

As we can see in figure 5, particle(s) at $\mathbf{x}=(x, y, z)$ are projected on the 2D image coordinate of the left camera, $(X^L, Y^L)=\mathbf{X}^L$, and of the right camera, $(X^R, Y^R)=\mathbf{X}^R$. Both image coordinates were computed with 3D-2D calibration functions, $\mathbf{X}^L=\mathbf{F}^L(x, y, z)$ and $\mathbf{X}^R=\mathbf{F}^R(x, y, z)$, which will be described in the following section.

Then, image displacement $\Delta\mathbf{X}^L$ and $\Delta\mathbf{X}^R$ of particle(s) at $\mathbf{X}^L$ and $\mathbf{X}^R$ were calculated respectively with regular PIV method in terms of direct cross-correlation between the small sub-domains (interrogation spot) of two successive images separated by time $\Delta t$. Next, the image coordinate of these points for the left camera was transformed back into the 3D physical coordinate (x, y, z) in forms

$$\begin{aligned}
\mathbf{x}_1^L &= \mathbf{f}_1^L(\mathbf{X}^L) \\
\mathbf{x}_2^L &= \mathbf{f}_2^L(\mathbf{X}^L) \\
\mathbf{x}_1^L + \Delta\mathbf{x}_1^L &= \mathbf{f}_1^L(\mathbf{X}^L + \Delta\mathbf{X}^L) \\
\mathbf{x}_2^L + \Delta\mathbf{x}_2^L &= \mathbf{f}_2^L(\mathbf{X}^L + \Delta\mathbf{X}^L).
\end{aligned} \tag{11}$$

For the right camera,

$$\begin{aligned}
\mathbf{x}_1^R &= \mathbf{f}_1^R(\mathbf{X}^R) \\
\mathbf{x}_2^R &= \mathbf{f}_2^R(\mathbf{X}^R) \\
\mathbf{x}_1^R + \Delta\mathbf{x}_1^R &= \mathbf{f}_1^R(\mathbf{X}^R + \Delta\mathbf{X}^R) \\
\mathbf{x}_2^R + \Delta\mathbf{x}_2^R &= \mathbf{f}_2^R(\mathbf{X}^R + \Delta\mathbf{X}^R).
\end{aligned} \tag{12}$$

where $\mathbf{f}$ is the mapping function from the 2D image coordinate of each camera to an $x$-$y$ plane at constant $z$ (where the surfaces of the calibration plate was located as shown in figure 5 in the 3D physical coordinate system. If the subscripts are 1, this means $z=z_1^L$ $(z_1^R)$. If the subscripts are 2, this means $z=z_2^L$ $(z_2^R)$. The superscript specifies the

## *3.2 Turbulence statistics*

Next, we turn to discussion on the turbulent statistics. Each of the following turbulent statistics were obtained from 50 independent series of velocity data: each series consists of 18 instantaneous volumetric velocity data measured with 0.446 s intervals. The mean and RMS velocity profiles are shown in figure 8. Here, $r$ is the radial distance from the jet's centerline estimated by fitting a 2D Gaussian function on the mean velocity data. The mean and RMS velocity were obtained by ensemble-averaging over all of the measured data. The profile was then computed by averaging in the azimuthal direction, and also by averaging in the streamwise direction over a range $x$=30$D$ to 50$D$, where the velocity profiles are self-similar, after normalizing with the half velocity width, $b$, and centerline mean velocity, $U_m$, at each streamwise station. Note that the centerline mean velocity at $x$=40$D$ was $U_m$=31.6 mm/s and the velocity half width was $b$=20.3 mm. Each mean and RMS velocity profiles had reasonable agreement with the data previously measured by Wygnanski and Fiedler (1969). The Reynolds stress $\overline{u'v'}$ was also shown in figure 9. Here, $u'$ and $v'$ are the fluctuations of azimuthal and radial velocity components. The Reynolds stress is averaged in the same way with the velocity profiles and normalized with the half velocity width, $b$, and square of centerline velocity, $U_m^2$. The profile of computed Reynolds stress agrees well qualitatively with the previous data by Wygnanski & Fiedoler (1969) and Ninomiya (1992), although the value itself is slightly larger. Such a quantitative difference might be occurred due to a lower Reynolds number of the present experiments than that of the previous one.

Figure 10 plots the ensemble RMS vorticity magnitude and ensemble RMS divergence. Both quantities were also square-summed over the $x$ direction within the measurement volume. The "filtered" RMS vorticity and RMS divergence, which were smoothed by averaging 3×3×3 nodes surrounding each node, were overlaid on the

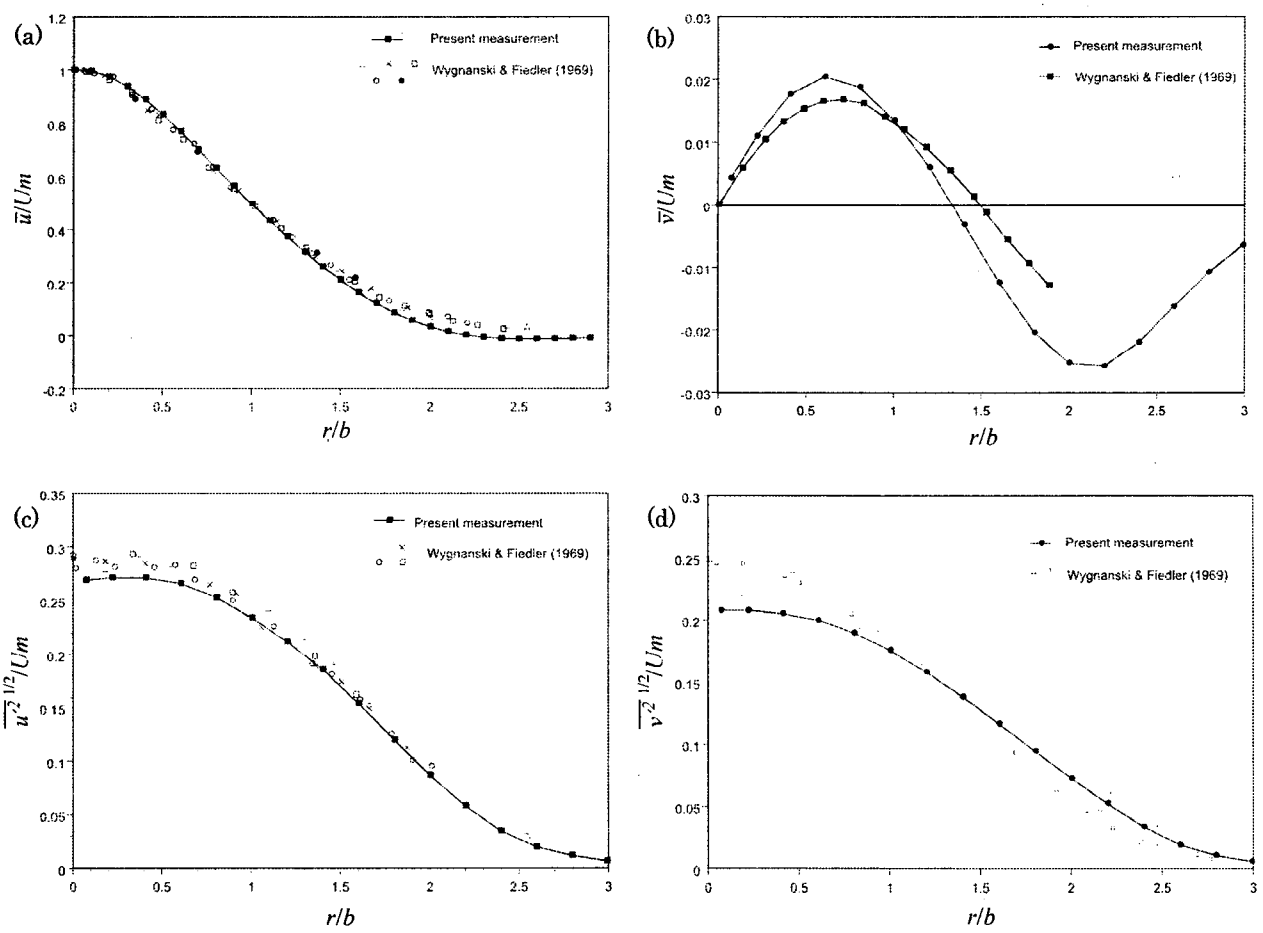


Figure 8. Turbulence statistics. (a)Mean velocity profile (azimuthal). (b)Mean velocity profile (radial). (c)RMS velocity profile (azimuthal). (d)RMS velocity profile (radial).

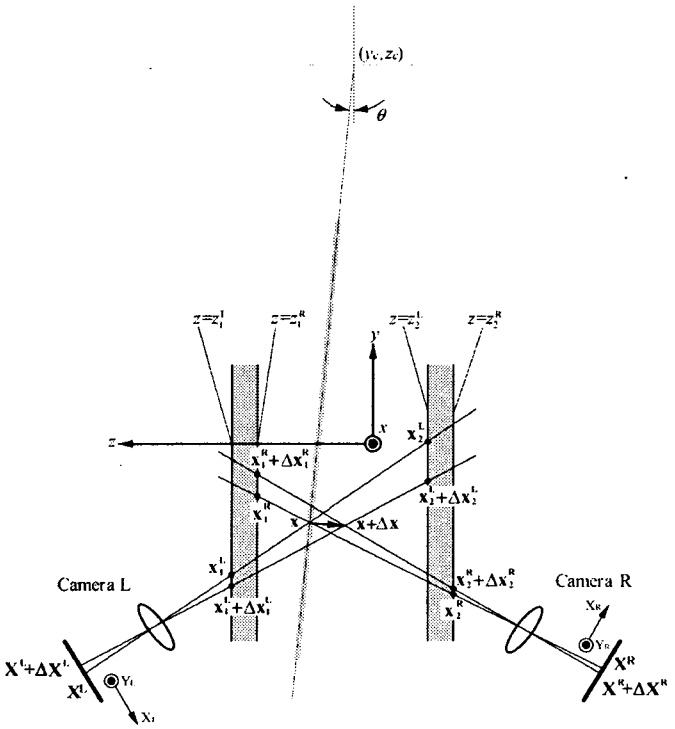


Figure 5. Projection of particle(s) onto the cameras. The light sheet plane (thin grey line) and calibration plates are also indicated.

camera. These mapping functions will also be described in the following section. Let us now calculate point $\mathbf{x}_{t0}$ where line $\mathbf{x}_1^L \rightarrow \mathbf{x}_2^L$ and line $\mathbf{x}_1^R \rightarrow \mathbf{x}_2^R$ intersect. Also calculate point $\mathbf{x}_{t1}$ where line $\mathbf{x}_1^L+\Delta\mathbf{x}_1^L \rightarrow \mathbf{x}_2^L+\Delta\mathbf{x}_2^L$ and line $\mathbf{x}_1^R+\Delta\mathbf{x}_1^R \rightarrow \mathbf{x}_2^R+\Delta\mathbf{x}_2^R$ intersect. Since two lines may not intersect due to errors in calibration functions or in measured particle displacement, we define "intersection" as the center of the smallest sphere to which both lines are tangential. Obviously, the two intersecting points, $\mathbf{x}_{t0}$ and $\mathbf{x}_{t1}$, are the three-dimensional positions of particle(s) at $t=0$ and $t=\Delta t$, respectively. Thus the velocity vector was obtained by

$$\mathbf{v} = (\mathbf{x}_{t1} - \mathbf{x}_{t0}) / \Delta t . \tag{13}$$

The size of the interrogation spot on the image plane of each camera was 28 × 28 pixels, which is approximately 2.7 × 3.9 mm$^2$ in $x$-$y$ physical plane.

## 2.6 Calibration

The calibration functions in the previous sections were obtained with the following procedure. First, a surface of the calibration plate facing to the camera L was placed at $z=z_1^L$, where the opposite surface of the plate was located at $z=z_1^R$ ($=z_1^L$-5 mm) as previously shown in figure 5. Note that $z_1^L$ ($z_1^R$) is not identical to the position of the plate set in section 2.3. The calibration grid images captured by the cameras were processed individually using following algorithms. Each grid point was searched with pattern matching, which found the peak location of the correlation of the original image and template pattern that was similar to the grid. After finding the location of each grid in the image coordinate, the physical location of each grid was determined automatically based on the location of the reference grid and the known spacing between the grids. This procedure produced a table of image coordinates and physical coordinates for the grid points, and created 2D-2D calibration function $\mathbf{f}_1^L$, $\mathbf{f}_1^R$ in the sense of the least squares method. Next, the calibration plate was traversed at $z=z_2^L$ ($z=z_2^R$), and a similar procedure produced another set of functions $\mathbf{f}_2^L$, $\mathbf{f}_2^R$. The form of the calibration function was based on a pinhole camera model with 2nd-order distortion (Willert, 1997), such as

$$\begin{pmatrix} x \\ y \end{pmatrix} = \mathbf{f}_\zeta^\Pi(X,Y) = \begin{pmatrix} \dfrac{a_0^{\Pi,\zeta} + a_1^{\Pi,\zeta}X + a_2^{\Pi,\zeta}Y + a_3^{\Pi,\zeta}X^2 + a_4^{\Pi,\zeta}Y^2 + a_5^{\Pi,\zeta}XY}{1 + a_{12}^{\Pi,\zeta}X + a_{13}^{\Pi,\zeta}Y + a_{14}^{\Pi,\zeta}X^2 + a_{15}^{\Pi,\zeta}Y^2 + a_{16}^{\Pi,\zeta}XY} \\ \dfrac{a_6^{\Pi,\zeta} + a_7^{\Pi,\zeta}X + a_8^{\Pi,\zeta}Y + a_9^{\Pi,\zeta}X^2 + a_{10}^{\Pi,\zeta}Y^2 + a_{11}^{\Pi,\zeta}XY}{1 + a_{12}^{\Pi,\zeta}X + a_{13}^{\Pi,\zeta}Y + a_{14}^{\Pi,\zeta}X^2 + a_{15}^{\Pi,\zeta}Y^2 + a_{16}^{\Pi,\zeta}XY} \end{pmatrix} \tag{14}$$

where index $\Pi$ denotes either $L$ or $R$ for identifying the camera, and index $\zeta$ denotes 1 if the plate location is $z=z_1^L$ ($z_1^R$) and denotes 2 if the plate location is $z=z_2^L$ ($z_2^R$). Coefficient $a_i^{\Pi,\zeta}$ was evaluated with the non-linear least-squares method.

Once these 2D-2D calibration functions were obtained, the remaining 3D-2D functions $\mathbf{F}^L$ and $\mathbf{F}^R$ were determined in the following way. Point $\mathbf{X}^\Pi$ in the image coordinate of camera $\Pi$ is a projection of all points on a line connecting $\mathbf{f}_1^\Pi(\mathbf{X}^\Pi)$ and $\mathbf{f}_2^\Pi(\mathbf{X}^\Pi)$. The intersection of this projection line and the measurement plane at angle $\theta$ is given by a function,

$$\mathbf{x}(\theta, \mathbf{X}^\Pi) = s[\mathbf{f}_2^\Pi(\mathbf{X}^\Pi) - \mathbf{f}_1^\Pi(\mathbf{X}^\Pi)] + \mathbf{f}_1^\Pi(\mathbf{X}^\Pi) \tag{15}$$

and

$$s = \frac{1 - c_1(\theta)y_1 - c_2(\theta)z_1^\Pi}{c_1(\theta)(y_2 - y_1) + c_2(\theta)(z_2^\Pi - z_1^\Pi)}, \tag{16}$$

where $(x_1, y_1, z_1^\Pi)=\mathbf{f}_1^\Pi(\mathbf{X}^\Pi)$ and $(x_2, y_2, z_2^\Pi)=\mathbf{f}_2^\Pi(\mathbf{X}^\Pi)$. The intersections for all $\theta$ values on which the measurement plane is located are found. Furthermore, these points are found for many possible $\mathbf{X}^\Pi$, and finally a set of data with many possible pairs of $\mathbf{X}^\Pi$ and $\mathbf{x}(\theta, \mathbf{X}^\Pi)$ can be prepared. This data was fitted into the following function based on a pinhole camera model with 2nd-order distortion using the non-linear least-squares method;

$$\begin{pmatrix} X \\ Y \end{pmatrix} = \mathrm{F}^\Pi \begin{pmatrix} x \\ y \\ z \end{pmatrix} = \begin{pmatrix} \dfrac{a_0^\Pi + a_1^\Pi x + a_2^\Pi y + a_3^\Pi z + a_4^\Pi x^2 + a_5^\Pi y^2 + a_6^\Pi z^2 + a_7^\Pi xy + a_8^\Pi yz + a_9^\Pi zx}{1 + a_{20}^\Pi x + a_{21}^\Pi y + a_{22}^\Pi z + a_{23}^\Pi x^2 + a_{24}^\Pi y^2 + a_{25}^\Pi z^2 + a_{26}^\Pi xy + a_{27}^\Pi yz + a_{28}^\Pi zx} \\ \dfrac{a_{10}^\Pi + a_{11}^\Pi x + a_{12}^\Pi y + a_{13}^\Pi z + a_{14}^\Pi x^2 + a_{15}^\Pi y^2 + a_{16}^\Pi z^2 + a_{17}^\Pi xy + a_{18}^\Pi yz + a_{19}^\Pi zx}{1 + a_{20}^\Pi x + a_{21}^\Pi y + a_{22}^\Pi z + a_{23}^\Pi x^2 + a_{24}^\Pi y^2 + a_{25}^\Pi z^2 + a_{26}^\Pi xy + a_{27}^\Pi yz + a_{28}^\Pi zx} \end{pmatrix} \tag{17}$$

# 3. Results

## 3.1 Instantaneous vortical structure

Let us begin our discussion on the measured data with the three-dimensional velocity vectors that have been reconstructed in figure 6. Here, only a few sections of the measurement domain have been displayed for clarity. The centerline of the jet is located near the center of the domain. The velocity vectors are raw results and no smoothing or enhancement has been done.

The vorticity vectors were computed with the 2nd order finite difference of the velocity vectors. Although the original measurement grids (nodes) were located on a non-parallel cylindrical coordinate, they were relocated to form parallel rectangular grids with a linear interpolation scheme prior to calculating vorticity for just convenience.

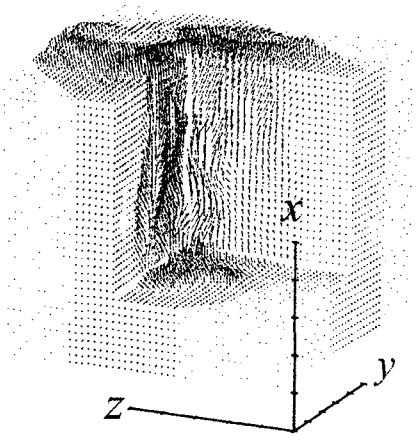


Figure 6. Three-dimensional view of instantaneous velocity vectors. Tick intervals are 10 mm in all directions.

Three-dimensional vortical structure, which is identified by vorticity, is visualized in figure 7. It revealed that the existence of a group of hairpin-like vortex structures was quite evident around the rim of the shear layer of the jet (Fig.7(a)). Figure 7(b) is overlaid with iso-surfaces of the radial component of velocity, $\tilde{v}_r$, where the red and blue surfaces indicate positive and negative values, respectively. It is obvious that the radial flows injecting outward through the inside of the hairpin and entrained to the rim of the structures. As shown in Fig.7(c), such an injecting flow induced by the hairpin vortex transfers the streamwise momentum outward, which indicates iso-surfaces of the instantaneous Reynolds shear stress. Many of the iso-surfaces of the Reynolds stress are located inside the hairpin loop, where the flow induced by the hairpin vortices transfers the high streamwise momentum in the core region of the jet toward the outer region. Although this type of hairpin vortices was already visualized by regurlar stereo-PIV by assuming Taylor's frozen field hypothesis (Matsuda & Sakakibara, 2005), direct measure of nine-component of velocity gradient tensor in the present study revealed more accurate feature of the structures, which is free from ambiguity arose from the assumption. Vorticity production associated with the stretching along local vorticity vector is indicated by color on the isosurfaces in Fig.7 (d). Some hairpin's head and legs are stretched and vorticity is amplified.

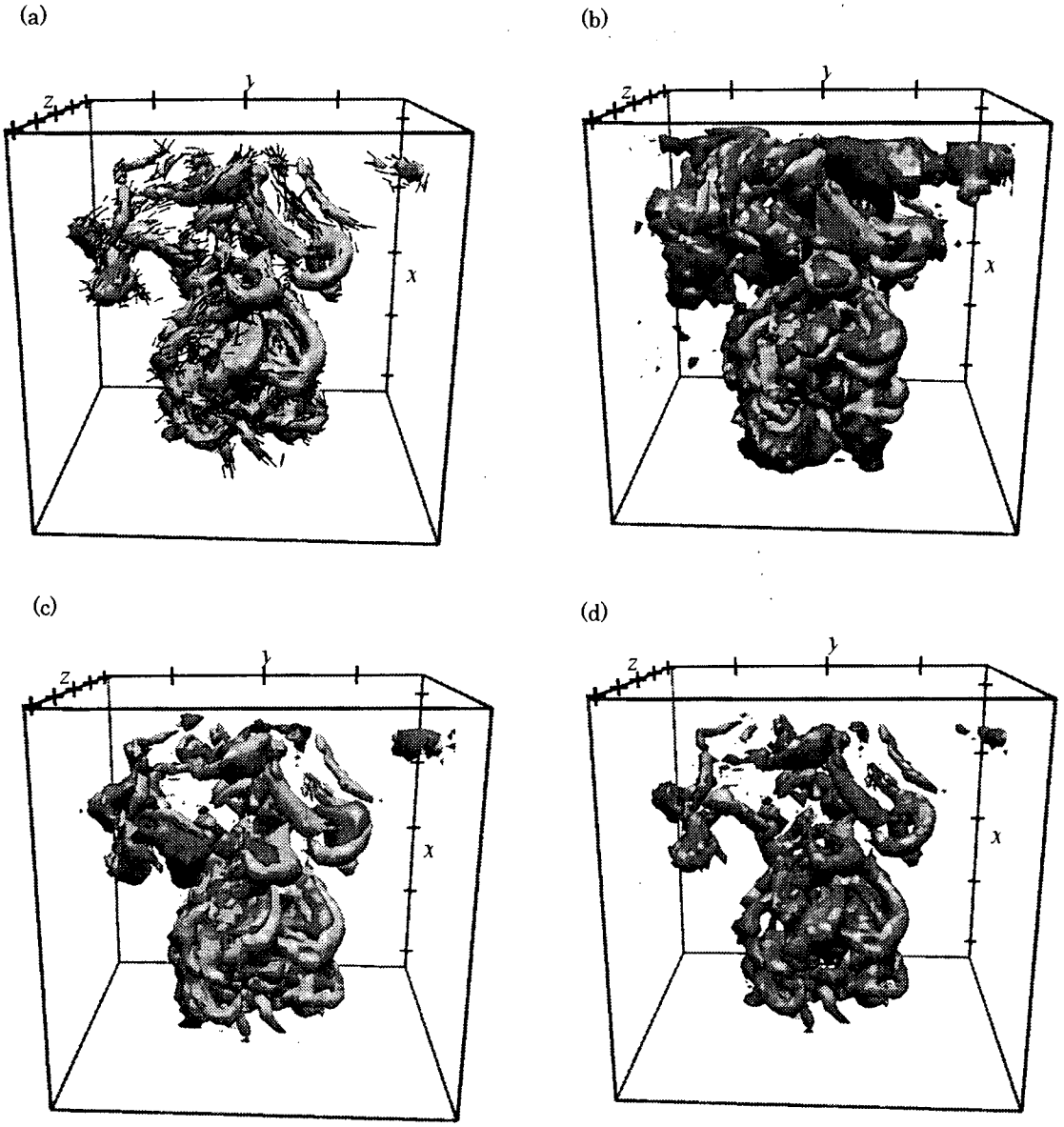


Figure 7 Surfaces of constant vorticity magnitude with (a) vorticity vectors, (b) isosurfaces of outward radial velocity, (c) isosurfaces of Reynolds shear stress, and (d) color indicating vorticity production.

## 3.2 Turbulence statistics

Next, we turn to discussion on the turbulent statistics. Each of the following turbulent statistics were obtained from 50 independent series of velocity data: each series consists of 18 instantaneous volumetric velocity data measured with 0.446 s intervals. The mean and RMS velocity profiles are shown in figure 8. Here, $r$ is the radial distance from the jet's centerline estimated by fitting a 2D Gaussian function on the mean velocity data. The mean and RMS velocity were obtained by ensemble-averaging over all of the measured data. The profile was then computed by averaging in the azimuthal direction, and also by averaging in the streamwise direction over a range $x$=30$D$ to 50$D$, where the velocity profiles are self-similar, after normalizing with the half velocity width, $b$, and centerline mean velocity, $U_m$, at each streamwise station. Note that the centerline mean velocity at $x$=40$D$ was $U_m$=31.6 mm/s and the velocity half width was $b$=20.3 mm. Each mean and RMS velocity profiles had reasonable agreement with the data previously measured by Wygnanski and Fiedler (1969). The Reynolds stress $\overline{u'v'}$ was also shown in figure 9. Here, $u'$ and $v'$ are the fluctuations of azimuthal and radial velocity components. The Reynolds stress is averaged in the same way with the velocity profiles and normalized with the half velocity width, $b$, and square of centerline velocity, $U_m^2$. The profile of computed Reynolds stress agrees well qualitatively with the previous data by Wygnanski & Fiedoler (1969) and Ninomiya (1992), although the value itself is slightly larger. Such a quantitative difference might be occurred due to a lower Reynolds number of the present experiments than that of the previous one.

Figure 10 plots the ensemble RMS vorticity magnitude and ensemble RMS divergence. Both quantities were also square-summed over the $x$ direction within the measurement volume. The "filtered" RMS vorticity and RMS divergence, which were smoothed by averaging 3×3×3 nodes surrounding each node, were overlaid on the

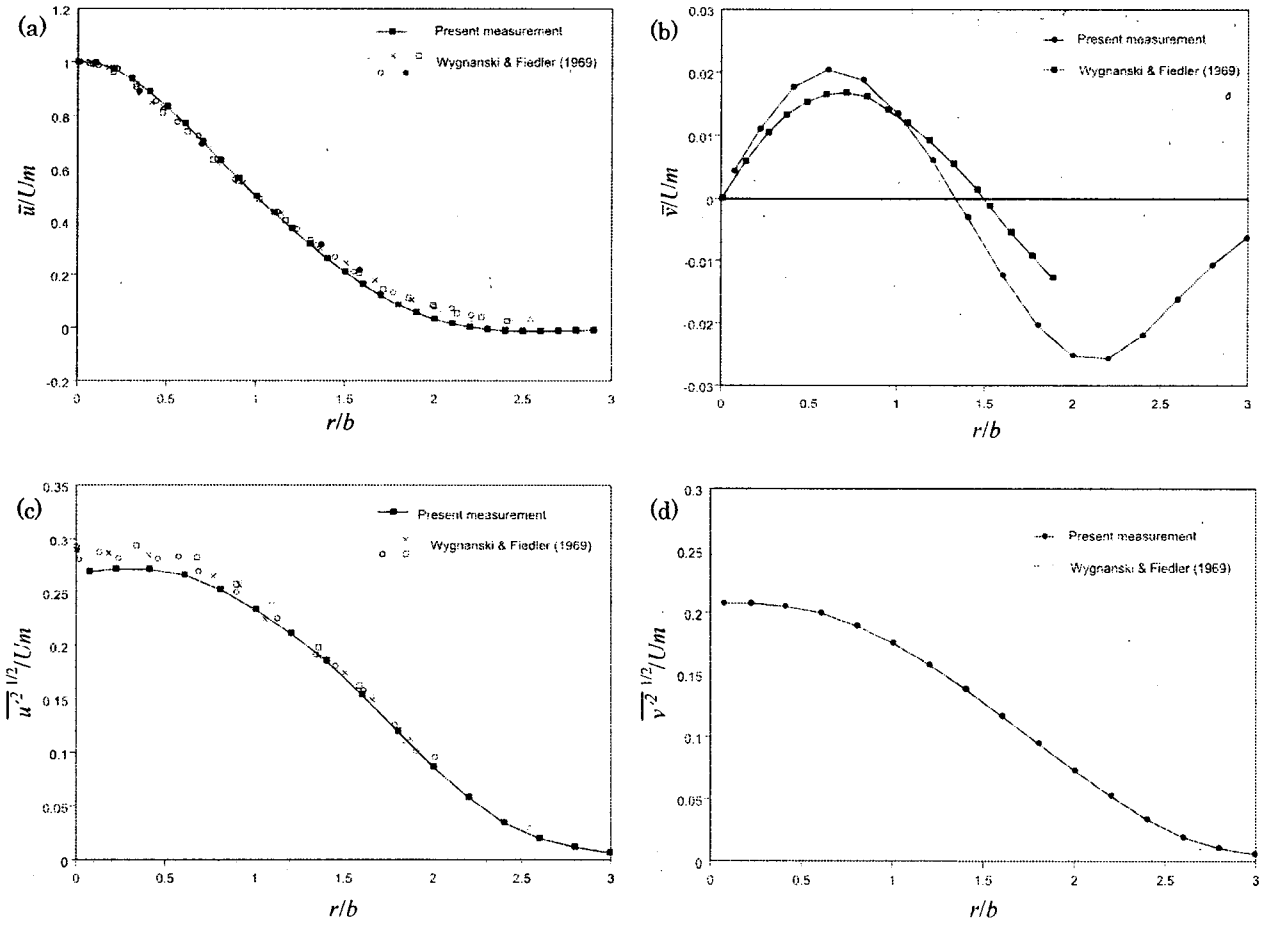


Figure 8. Turbulence statistics. (a)Mean velocity profile (azimuthal). (b)Mean velocity profile (radial). (c)RMS velocity profile (azimuthal). (d)RMS velocity profile (radial).

figure. Both divergences have a maximum at $r$=0, where the vorticities are also largest. The ratio between "raw" RMS vorticity and RMS divergence at $r$=0 was approximately 0.22. Meanwhile, the ratio of "filtered" was 0.07. The "filtered" divergence was reasonably small to capture the large-scale vortical structures.

# 4. Conclusion

We developed scanning stereo-PIV system to measure the three-dimensional distribution of three-component velocity in a turbulent round jet. A laser light sheet produced with a high-repetition-rate YLF pulse laser was scanned with an optical scanner. The evolution of the mirror angle had the form of a linear slope with small amplitude oscillations, which allowed more freedom in choosing the time interval $\Delta t$ of a pair of particle images. Two high-speed mega-pixel resolution C-MOS cameras captured the particle images illuminated by the light sheet, and we adopted new stereoscopic PIV method to acquire the 3D-3C-velocity distribution of a turbulent water jet that was formed by a round nozzle with an exit diameter of $D$=5 mm. The jet Reynolds number was set at $Re \approx$ 1000, and the streamwise location of the center of measurement volume was fixed at approximately $x$=40$D$, where the centerline mean velocity was approximately 31.6 mm/s.

The measurement volume ($\approx$ 100×100×100 mm$^3$) containing 50 velocity planes was scanned in 0.216 s, which was sufficiently short to capture instantaneous vortical structures. Iso-vorticity surfaces clearly showed hairpin structures on the rim of the shear layer. The turbulence statistics was good agreement with the previous data. The divergence of the filtered (unfiltered) velocity field was approximately 7% (22%) of rms vorticity on the centerline of the jet.

# Acknowledgement

We are grateful to Prof. H. Hayami of Kyusyu University, the leader of Dynamic PIV Project, for his cooperation and Mr. S. Aramaki of the same university for his assistance with the experiments. We also wish to thank the project members, Dr.K.Okamoto of Tokyo University, Dr.K.Nishino of Yokohama National University, Dr.M.Kawahashi of Saitama University, and Dr.T.Kobayashi of the Japan Automobile Research Institute for their helpful discussions. Further, Mr.T.Nakajima and Mr.F.Yamada in University of Tsukuba are gratefully acknowledged for designing and machining hardwares needed for optical scanner system. The experiments were conducted at the Institute for Materials Chemistry and Engineering of Kyushu University, Japan. This work was partly supported by a Grant-in-Aid (No. 14205031) for Scientific Research by Japan Society of Promotion for Science.

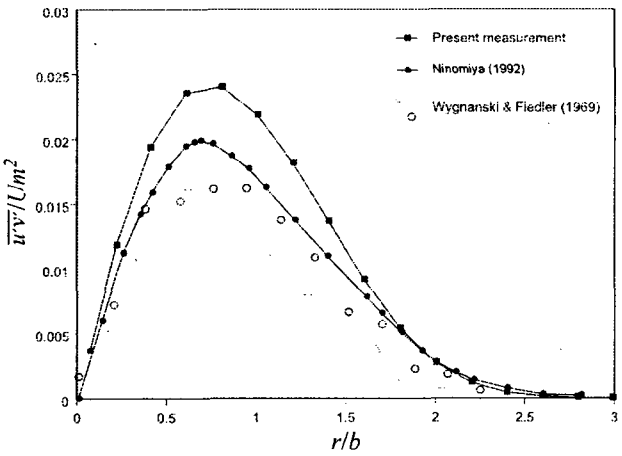


Figure 9. Radial distribution of Reynolds stress.

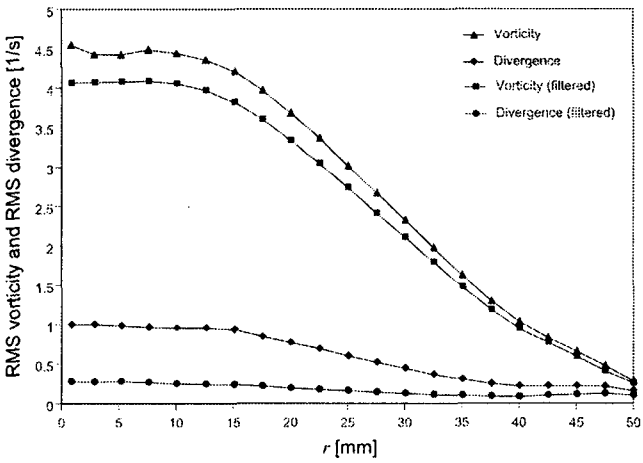


Figure 10. Ensemble rms vorticity magnitude and ensemble rms divergence.

# References


Brucker C 1995 Digital-Particle-Image-Velocimetry (DPIV) in a scanning light-sheet: 3-D starting flow around a short cylinder *Exp. Fluids* **19** 255-63

Brucker C 1996 3-D Scanning-Particle-Image-Velocimetry: Technique and Application to a Spherical Cap Wake Flow *Applied Scientific Research* **56** 157-79

Chiu W C and Rib L N 1956 The rate of dissipation of energy and the energy spectrum in a low-speed turbulent jet *Trans. Am. Geophys. Union* **37** 13-26

Hori T and Sakakibara J 2004 High-speed scanning stereoscopic PIV for 3D vorticity measurement in liquids *Meas. Sci. Technol.* **15** 1067-78

Matsuda, T., Sakakibara, J., 2005, "On the vortical structure in a round jet", *Physics of Fluids*, **17**, 2, to be published.

Nedderman R M 1961 The use of stereoscopic photography for the measurement of velocities in liquids *Chem. Eng. Sci,* **16** 113-9

Ninomiya N 1992 Ph.D thesis, University of Tokyo

Nishino K, Kasagi N and Hirata M 1989 Three-dimensional particle tracking velocimetry based on automated digital image processing *Trans. ASME, J.Fluids Eng.* **111** 384-91

Recca R G and Dewey J M 1988 A method for automatic particle tracking in a three-dimensional flow fluid *Exp. Fluids* **6** 25-32

Stitou A and Riethmuller M L 2001 Extension of PIV to super resolution using PTV *Meas. Sci. Technol.* **12** 1398-1403

Ushijima S and Tanaka N 1996 Three dimensional particle tracking velocimetry with laser light sheet scannings *Trans. ASME J.Fluids Eng* **118** 352-7

Willert C 1997 Stereoscopic digital particle image velocimetry for application in wind tunnel flows *Meas. Sci. Technol.* **8** 1465-79

Wygnanski I and Fiedler H 1969 Some measurements in the self-preserving jet *J. Fluid Mech* **38** 577-612

Zhang J, Tao B and Katz J 1997 Turbulent flow measurement in a square duct with hybrid holographic PIV *Exp. Fluids* **23** 373-381